Plasmon damping and charge transfer pathways in Au@MoSe2 nanostructures

I. Abid, P. Benzo, B. Pécassou, S. Jia, J. Zhang, J. Yuan, Jean Baptiste B Dory, Olivier Gauthier-Lafaye, Renaud Péchou, Adnen Mlayah, et al.

Plasmon damping and charge transfer pathways in Au@$MoSe_2$ nanostructures

Ines Abid,[1] Patricio Benzo,[1] Béatrice Pécassou,[1] Shuai Jia, [3] Jing Zhang, [3] Jiangtan Yuan, [3] Jean Baptiste Dory,[1,2] Olivier Gauthier Lafaye,[2] Renaud Péchou,[1] Adnen Mlayah,[1,2b]* Jun Lou[3]*

[1] *CEMES, Université de Toulouse, CNRS, UPS, Toulouse, France*
[2] *LAAS, Université de Toulouse, CNRS, UPS, Toulouse, France*
[3] *Department of Materials Science and NanoEngineering, Rice University, Houston Texas 77005, USA*

Hybridization of plasmonic and excitonic elementary excitations provides an efficient mean of enhancing the optical absorption and emission properties of metal/semiconductor nanostructures and is a key concept for the design of novel efficient optoelectronic devices. Here we investigate the optical properties of 2D $MoSe_2$ quantum well flakes covered with Au nanoparticles supporting plasmonic resonances. Using spatially resolved confocal spectroscopy, we report the observation of a quenching phenomenon of the Raman scattering and photoluminescence emission of both the $MoSe_2$ layer and the Au nanoparticles. We found that the quenching of the photoluminescence emission from the Au nanoparticles is partial and measurable unlike the one observed for the Au-covered $MoSe_2$ layers, which is total. Its dependence on the thickness of the $MoSe_2$ layer is determined experimentally. Based on electro-dynamics calculations and on the electronic band alignment at the Au/ $MoSe_2$ interface, the results are interpreted in terms of i) damping of the plasmonic resonance of the Au nanoparticles due to the optical absorption by the $MoSe_2$ layer ii) a two-pathways charge transfer scheme where the photo-excited electrons leak from the $MoSe_2$ layer to the Au NPs whereas the photo-excited holes flow in the opposite direction i.e., from the Au NPs to the $MoSe_2$ layer. The two combined mechanisms account well for the experimental observations and complements the interpretations proposed in the literature for similar metal nanoparticles/transition metal dichalcogenide systems.

Keywords: hybrid plasmonic, 2D materials, charge transfer, Plasmon damping, Photoluminescence quenching

Introduction

Combining two-dimensional (2D) semiconductor quantum wells (QWs) made of single layers of transition metal dichalcogenides (TMDs) and plasmonic nanomaterials opens up new routes to investigate plasmon-exciton interaction [1–5] and to engineer highly efficient and functional hybrid nanodevices in the field of electronics [6–8], photovoltaics [9], sensing [10-11], integrated photonic-electronic circuit [12] and photocatalysis [13–15]. In this context, exploring the contact interface between the metal nanostructures and the TMD layers is crucial to understand the optical, structural and mechanical properties of these hybrid systems. Recent studies proved that the deposition of metal nanoparticles on TMDs may modify the electronic, optical and vibrational properties of the TMD layer [16–22]. Gong et al [16] showed that the optical phonons are very sensitive to the nature of the deposited metal NPs and to the surface coverage. Using surface enhanced raman scattering (SERS), Sun et al [22] and Zhang et al [18] pointed out strain effects induced by the metallic nanoparticles

deposited on MoS_2 layers. A quenching phenomenon of the PL emission in monolayer TMDs has been first reported by Bhanu et al [21] in Au/MoS_2 flake. They showed that because the electron affinity of MoS_2 is lower than the work function of Au, the photo-excited electron in the MoS_2 layer readily transfer to the Au, leaving the hole behind. This Charge Transfer (CT) mechanism strongly reduces the probability for radiative recombination and causes PL quenching.

Actually, the phenomenon of PL quenching in monolayers of transition metal dichalcogenides has various origins. i) Kang et al [23] investigated the effect of plasma oxygen treatment on the optical properties of single layer MoS_2 and have demonstrated the creation of MoO3 defect sites controlled by the plasma exposure time. They showed that such defects are responsible for lattice distortion and local direct-to-indirect band gap transition causing phonon assisted exciton recombination and PL quenching. ii) Yuan et al [24] studied the interlayer coupling behaviour of bilayer stacked MoS_2, WS_2 and MoS_2/WS_2 heterostructures with varied stacking order. They demonstrated that the strong PL quenching is due to the exciton splitting and to the subsequent reduction of the radiative recombination probability due to both the type-II band alignment and the build-in electric field in these heterostacks. iii) Kim et al [25] studied the PL quenching in Al_2O_3 encapsulated MoS_2, $MoSe_2$, WS_2 and WSe2 monolayers. Using bottom gated photo-transistors, they showed that the photo-current and the responsivity were increased after Al_2O_3 encapsulation. These experimental findings were interpreted in terms of hole transfer from the TMD layer to encapsulation-induced trap states. iv) Recently Zhang et al [26] reported giant PL quenching factors of nearly 3.5 and 10 in respectively MoS_2/Au and MoS_2/Pd heterolayers at liquid nitrogen temperature. The quenching phenomenon was interpreted in terms of interlayer CT governed by temperature and by Van der Waals interlayer interaction along the lines proposed by Bhanu et al [21].

The PL quenching phenomenon in hybrid metal/TMD nanostructures may have a strong impact on future applications and can even be put to good use in novel optoelectronic designs. For instance, one may seek for total suppression of the radiative recombination of electron-hole pairs in monolayer TMDs for optimum light-to-current conversion and enhanced responsivity of photodetectors. On the other hand, from a fundamental point of view, understanding the dynamics of the CT between plasmonic metal nanoparticles and TMDs layers and its impact on the optical properties is still on the way and requires further experimental and theoretical studies. In this work, we systematically investigate the optical properties of $MoSe_2$ layers covered with Au nanoparticles. Among the family of 2D TMD materials, $MoSe_2$ has the advantage of a fundamental excitonic absorption around 800 nm (A exciton) [27,28], red-shifted with respect to the interband absorption of Au, thus minimizing the excitation transfer from the TMD layer to the Au NPs and the resulting dissipation effects. Using spatially resolved PL and Raman measurements, we investigate the phenomenon of PL emission and Raman scattering quenchings of both the $MoSe_2$ layer and the Au NPs. The study is however focused on the quenching of the PL emission from the Au NPs. Indeed, to the best of our knowledge, up to now, only the PL quenching of TMD layers combined with various metallic materials has been addressed in the literature [21,23-26], as stated above, and interpreted in terms of CT across the metal/semiconductor interface. Here, we show that the analysis of the PL signal emitted by both the $MoSe_2$ layer and the Au NPs brings valuable information which allows for a deeper understanding of the optical properties of this hybrid nanostructure and of the CT mechanisms taking place at the metal/semiconductor interface.

Sample preparation

The $MoSe_2$ flakes were grown by chemical vapor deposition (CVD) on a SiO_2 (90 nm)/Si substrate. The latter was exposed to MoO3 and pure selenium powder at high temperature (750 °C), thus leading to the nucleation and the growth of large crystalline area of multilayer and monolayer $MoSe_2$ flakes [29,30]. The Au NPs were deposited at a deposition rate of 0.027 nm/s on the $MoSe_2$ layers by magnetron sputtering of a pure gold target in ultra-high-vacuum at 600°C. Part of the SiO_2 /Si substrate supporting the $MoSe_2$ flakes was protected from the sputtered Au atoms flow by a mask and has been later used as a reference for the uncovered $MoSe_2$ flakes, and to investigate the change of the optical properties with Au NPs density (i.e., with surface coverage). Indeed, in the transition zone between Au-covered and bare regions of $MoSe_2$, the Au NPs density progressively decreases as will be shown later. In this study, two equivalent thicknesses of Au (i.e., the thickness of a 2D layer with same volume) were investigated: 4.8 and 0.8 nm. The average size of the Au NPs obtained with 4.8 and 0.8 nm equivalent thicknesses are, respectively, 17 and 7 nm as determined by Scanning Electron Microscopy (SEM) imaging (Figure A1 Appendix).

Results and discussion

Scanning Electron Microscopy (SEM) and Atomic Force Microscopy (AFM) images (Figure 1) show that the Au nanoparticles form separated clusters, when deposited either on SiO_2 or on $MoSe_2$. This suggests a Volmer-Weber growth mode of Au on both surfaces, in agreement with previously reported works on Au and Ag NPs deposited on MoS_2 [16,19]. As a matter of fact, it has been shown earlier that Au grows epitaxially on MoS_2 [31] and as a result the Au NPs display a flat surface [32–34]. One can also notice (Figure 1C, E) that the size and density of the NPs depend on the nature of the supporting surface. Indeed, the nanoparticles formed on $MoSe_2$ are larger and denser than those formed on SiO_2. The estimated surface coverage is 62% for Au NPs on monolayer $MoSe_2$ and only 40 % on SiO_2. This difference in surface coverage can be attributed to the amorphous nature of the SiO_2 substrate which prevents the growth and coalescence of adjacent Au seeds required to form large metallic Au nanoparticles and to increase the surface coverage. Moreover, Figure 1C, E show that the NPs size and density depend on the thickness of the $MoSe_2$ layer as well. Indeed, they both increase with increasing $MoSe_2$ layer thickness as already reported by Deng et al [19] for Ag NPs on MoS_2.

Optical absorption measurements under confocal microscope were performed on the $MoSe_2$@ SiO_2 and Au@ SiO_2 samples. A surface plasmon (SP) resonance is observed around 580 nm on both Au@ SiO_2 samples deposited with 4.8 and 0.8 nm equivalent thicknesses (Figure A2 Appendix). Its large spectral width (around 150 nm at half maximum) is due to the size-dependent broadening of the SP resonance and to the near-field electromagnetic interaction between the Au NPs separated by nanometer gaps [35].

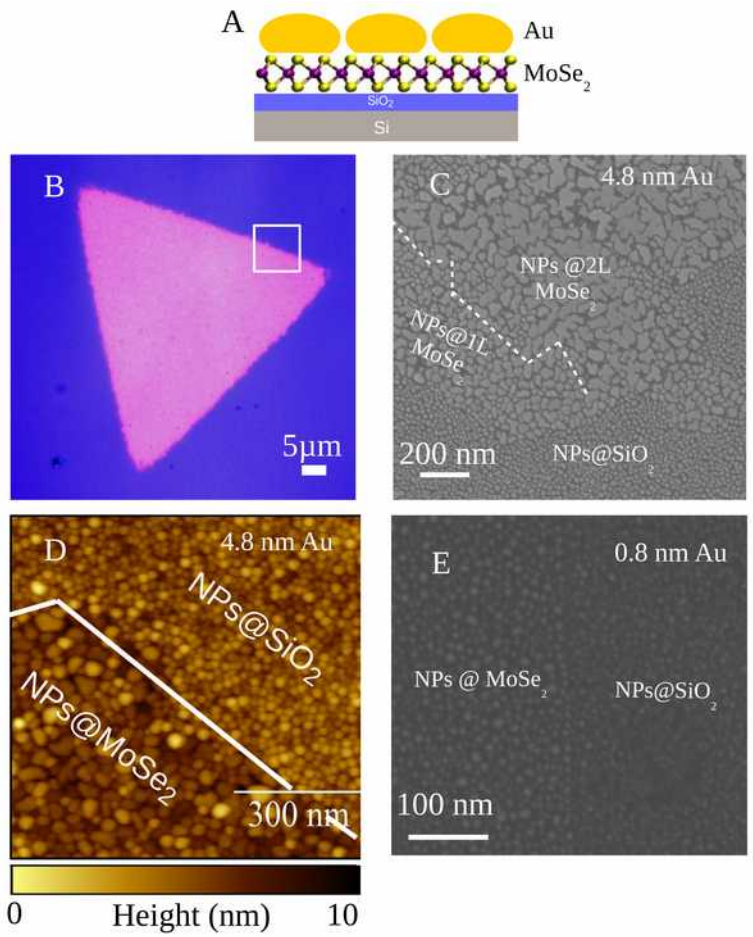

Figure 1: A) Cross-section drawing of the sample. B) Optical microscopy image C) SEM and D) AFM topography images of a $MoSe_2$ flake covered by Au NPs deposited with 4.8 nm Au equivalent thickness. E) SEM image of a $MoSe_2$ flake covered by Au NPs deposited with 0.8 nm Au equivalent thickness.

The optical absorption spectrum of $MoSe_2$@ SiO_2 exhibits two maxima around 800 and 700 nm (Figure A2, Appendix) due to the A and B exciton transitions, respectively [27,28]. To investigate the effect of the deposited Au NPs on the optical properties of the $MoSe_2$ layer, we have performed spatially resolved PL measurements. The PL signal from the bare $MoSe_2$ region is used as a reference. As shown in Figure 2A, the PL emission from the bare $MoSe_2$ region is characterized by a strong emission peak at 820 nm, due to the radiative recombination of the lower energy A excitons, and is very typical of a direct-band gap $MoSe_2$ monolayer [27-30].

Interestingly, this prominent PL emission completely disappeared in the case of $MoSe_2$ monolayer covered with Au NPs, suggesting a strong PL quenching phenomenon (Figure 2A). In order to determine the origin of this remarkable effect, three main hypotheses can be invoked: i) the absorption of the $MoSe_2$ luminescence emission by the Au NPs, ii) the possible presence of a tensile strain generated by the growth of the Au NPs on the $MoSe_2$ layer, iii) the separation of the photo-generated electrons and holes due to CT between the $MoSe_2$ layer and the Au NPs.

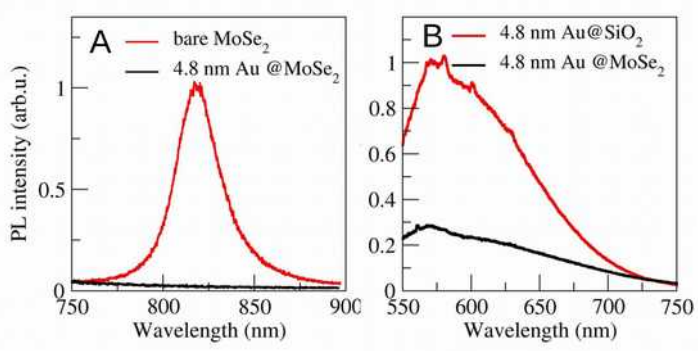

Figure 2: A) Room-temperature PL spectra of bare (red) and 4.8 nm equivalent thickness Au NPs-covered $MoSe_2$ monolayer (black). B) PL spectra of 4.8 nm equivalent thickness Au NPs deposited on SiO_2 (red) and on $MoSe_2$ (black). The PL emission was excited by a 532 nm laser.

To investigate the role of the optical absorption by the Au NPs, the measurements were reproduced for a smaller deposited Au thickness (0.8 nm equivalent thickness, i.e., 7 nm average NPs size), in order to reduce the overall optical density of the Au NPs. As shown in Figure A3A (Appendix), no PL emission from the $MoSe_2$ monolayer covered with Au NPs was detected in this case and the quenching effect remained total. Moreover, the excitation laser intensity has been increased by a factor 100 to enhance the photo-generation of electron-hole pairs in the $MoSe_2$ layer. Even so, no PL emission was detected at all (Figure A3B) which points out the high efficiency of the mechanism responsible for the PL quenching. The latter being independent of the Au NPs optical density, the absorption of the $MoSe_2$ PL emission by the Au NPs can be ruled out to account for the observed PL quenching of $MoSe_2$.

Several studies [16,36–44] showed that the strain imposed by the metal NPs to the TMD layer may strongly modify its electronic band structure and can be responsible for a strong quenching of the PL emission. In particular, tensile strain may induce a direct-to-indirect band gap transition [37,41,42] which leads to a red shift of the PL peak and to a drastic decrease of the PL intensity [38,39,42,43]. Using calculations based on Density Functional Theory (DFT), Horzum et al [37] showed that monolayer $MoSe_2$ undergoes a direct-to-indirect band gap crossover under ∼3% biaxial tensile strain. In our samples, strain could be generated for two main reasons: i) the 24% lattice mismatch between $MoSe_2$ and Au, and/or ii) the cooling of the sample from the rather high growth temperature (600°C) of the Au NPs down to room temperature, which may generate tensile stress and strain in the $MoSe_2$ layer because of the different thermal expansion coefficients of Au and $MoSe_2$@ SiO_2 substrate. To track the presence of strain in our Au@ $MoSe_2$ layers, we have performed Raman spectroscopy measurements. As shown in Figure A4 (Appendix), the intensity of the $MoSe_2$ Raman peaks due to the A'_1 phonons vanishes for 4.8 nm equivalent thickness Au@ $MoSe_2$ sample. However, for 0.8 nm deposited thickness, the Raman signature of the A'_1 mode remains visible and red-shifted by 5.7 cm^{-1}. According to the calculations performed by Horzum et al [37], the A'_1 vibration frequency is lowered by 9 cm^{-1} for a 1% biaxial tensile strain. The 5.7 cm^{-1} red-shift measured in our samples corresponds thus to 0.6% strain which is a rather moderate value consistent with the slow cooling rate of the sample (24°/min in the initial 20 min and 1.3°/min at longer times) after Au NP deposition at 600°C. This value is well below the 3% minimum strain required for the direct-to-indirect band-gap transition in monolayer $MoSe_2$. Nevertheless, the PL of monolayer $MoSe_2$ is totally quenched in our samples. Therefore, it is unlikely that,

although present, the tensile strain plays a significant role in the total quenching of the PL emission.

The quenching of the PL emission from the metal/TMD nanostructures has already been reported in the literature [21,26] and was interpreted as due to the transfer of photo-excited electrons from the TMD layer to the metal NPs. In our $MoSe_2$/Au nanostructures, the observed quenching is so strong that it is not even measurable as no PL emission from the monolayer $MoSe_2$ could be detected even at liquid nitrogen operation temperature and at high optical pumping rate (Figure A3 Appendix).

In order to further reduce the density of Au NPs and force the emergence of the PL emission from the $MoSe_2$ layer, we have performed spatially resolved PL measurements on $MoSe_2$ flakes partly covered by a mask prior to the deposition of Au (0.8 nm equivalent thickness). In this way, the density of the deposited Au NPs decreases continuously across the transition area between Au-covered and bare regions of the $MoSe_2$ flake (Figure A5, Appendix). As expected, the PL emission of the monolayer $MoSe_2$ and the Raman scattering by A'_1 phonons emerge with decreasing density of Au NPs (Figure A6 Appendix), i.e., density of trap sites for the photo-generated electrons. It is worth to underline that quenchings of both PL emission and Raman scattering are observed (Figures A5 and A6 Appendix) on Au NPs-covered $MoSe_2$ monolayer which suggests a common fundamental mechanism as will be discussed below.

The transfer of photo-excited electrons from the TMD layer to the metal NPs gives a satisfactory interpretation of the quenching of the PL emission of the $MoSe_2$ monolayer and will be discussed below in more detail. However, so far, the investigations were focused on the PL emission of the TMD layer solely. The PL emission of the Au NPs has been disregarded up to now. Although much weaker than the PL emission of the TMD layer, the PL emission of the Au NPs brings valuable information on the CT phenomena as will be seen now.

The PL emission of Au NPs is due to radiative recombinations of the photo-generated conduction electrons above the Fermi level with holes mainly in the d valence band which is characterized by a large density of states. The PL emission is very broad: it spans from 550 to 770 nm [45–47] as observed in the spectrum of the Au NPs deposited on SiO_2 (Figure 2B). This is due to the electronic band structure of gold and to the convolution of the emitted spectrum by the broad SP resonance of the Au NPs (Figure A2 Appendix).

Surprisingly, the PL emission intensity (integrated over the entire spectral range and excluding the Raman peaks) of the Au NPs covering the $MoSe_2$ flake is around 34% of that observed for the Au NPs supported by the SiO_2 surface (Figure 2B). This quenching is only partial and not total as the one observed for the emission of monolayer $MoSe_2$ (Figure 2A). It is measurable and thus can be exploited to investigate the PL quenching mechanism.

Figure 3A displays an optical microscope image of a multilayer $MoSe_2$ flake covered with Au NPs (4.8 nm equivalent film thickness). The thickness of the flake increases from region b to f as shown by the increasing optical contrast. Region a, where the Au NPs cover the SiO_2 substrate, is used as a reference. As shown in Figure 3B, the PL emission is reduced by nearly a factor 3 in region b (monolayer $MoSe_2$) and by a factor 100 in region f (bulk-like $MoSe_2$). This indicates that the PL quenching of the Au NPs is strongly influenced by the thickness of the MoSe2 supporting layer.

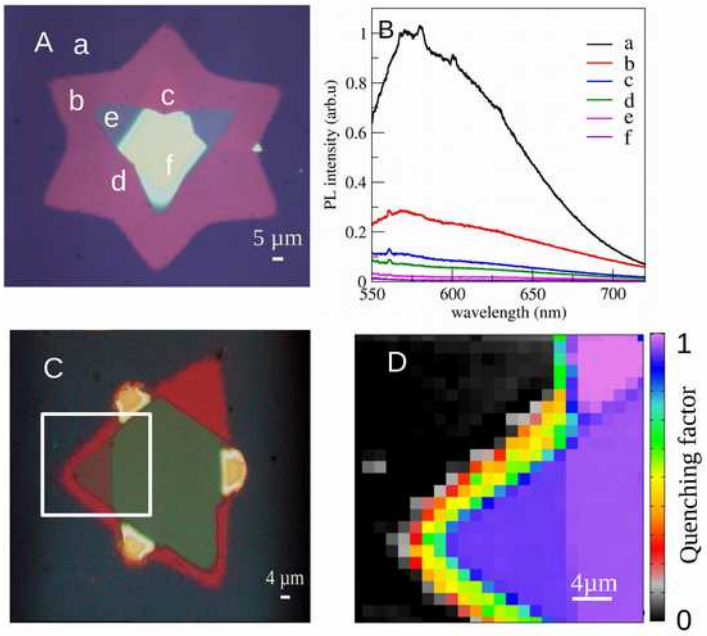

Figure 3: A, C) Bright field optical microscopy images of two multilayer $MoSe_2$ flakes covered by Au NPs with 17 nm average size (i.e., 4.8 nm equivalent thickness). B) PL spectra of the Au NPs recorded in the regions labelled a to f in A. The sharp peaks below 550 nm correspond to the Raman scattering by the Si optical phonon of the SiO_2 /Si substrate and by the A'_1 optical phonons of the $MoSe_2$ layer. D) Map of the quenching factor Q of the PL emission of the Au NPs in the region delimited by the square shown in C.

We here define a quenching factor of the PL emission of the Au NPs as

$$Q(x,y) = 1 - \frac{I_{PLAu@MoSe_2}(x,y)}{\langle I_{PLAu@SiO_2} \rangle} \qquad (1)$$

Where $I_{PLAu@MoSe_2}(x, y)$ is the measured local PL intensity of the Au NPs covering the $MoSe_2$ flake integrated in the 550-720 nm spectral range. $\langle I_{PLAu@SiO2} \rangle$ is the spatially averaged PL intensity of the Au NPs covering the SiO_2 surface integrated in the same spectral range and used as a reference. As defined, the quenching factor Q is equal to 1 when the PL of the Au NPs on $MoSe_2$ is completely quenched, and 0 when the photoluminescence of Au NPs on $MoSe_2$ and on SiO_2 are identical. It is worth to mention that the quenching factor as defined by Eq.1 is obtained from the raw PL data regardless of the different density (i.e., surface coverage) and surface morphology of Au NPs deposited on $MoSe_2$ and on SiO_2 (Figure 1C, E).

Knowing that the photoluminescence of Au NPs films similar, to those studied here, strongly depends on the surface roughness and grain boundaries formed on the nanoparticle surface46 and keeping in mind that the average NPs density are larger on $MoSe_2$ than on SiO_2 (Figure 1C, E), the actual quenching factor is larger than the one estimated using Eq.1. For instance, the quenching factor for Au NPs deposited on one monolayer $MoSe_2$ is 66% (Figure 2B) but reaches 78% when corrected for the different surface coverages (62% for Au NPs on $MoSe_2$ and 40% for Au on SiO_2, Figure 1C, E).

As shown in Figure 1C, the surface coverage, Au NPs size, and surface roughness and morphology also depend on the thickness of the $MoSe_2$ layer supporting the nanoparticles. In order to avoid uncertainties in the estimation of the quenching factor which may arise from corrections due to thickness dependent surface coverage and

surface roughness inhomogeneities, we use the definition of the quenching factor given by Eq.1.

To investigate the dependence of the quenching on the $MoSe_2$ layer thickness, we present in Figure 3D a systematic mapping of the quenching factor generated from spatially resolved PL measurements performed on another multilayer $MoSe_2$ flake covered with Au NPs and displayed in Figure 3C. The map of the quenching factor Q (Figure 3D) clearly matches the optical image of Figure 3C and confirms the increase of the quenching efficiency with increasing thickness of the $MoSe_2$ layer flake.

It is worth to mention that because of the presence of Au NPs on the $MoSe_2$ flake, the AFM height profile cannot provide the thickness of the $MoSe_2$ flake. Indeed, typical size of the Au NPs is around 17 nm whereas the thickness of a $MoSe_2$ single layer is 0.8 nm [29]. Therefore, it is impossible to extract the layer thickness from AFM profiles due to the large height fluctuations. To determine the thickness of covered $MoSe_2$ flakes we rather rely on optical methods. Indeed, to determine the thickness of $MoSe_2$ flakes, we exploit the Raman signal of the Si phonons from the Si/SiO_2 substrate. The number of $MoSe_2$ monolayers has been evaluated by using Beer-Lambert's law which accounts for the laser absorption by the $MoSe_2$ flake and for the subsequent decrease of the Si Raman peak intensity with increasing flake thickness. We also assumed that the region with the minimum optical contrast (region b in Figure 3A) is a monolayer thick $MoSe_2$ as shown by the strong PL emission exhibited by regions of similar optical contrast.

Figure 4 displays, now quantitatively, the dependence of the quenching factor Q on the thickness of the $MoSe_2$ multilayer flake. It increases from 66% for Au NPs on monolayer $MoSe_2$ to 96% when the nanoparticles are supported by approximately 40 monolayers thick $MoSe_2$. The measured maximum value 99.6% is reached for Au NPs supported by bulk-like $MoSe_2$ (around 143 monolayers thick as estimated from Beer-Lambert's law).

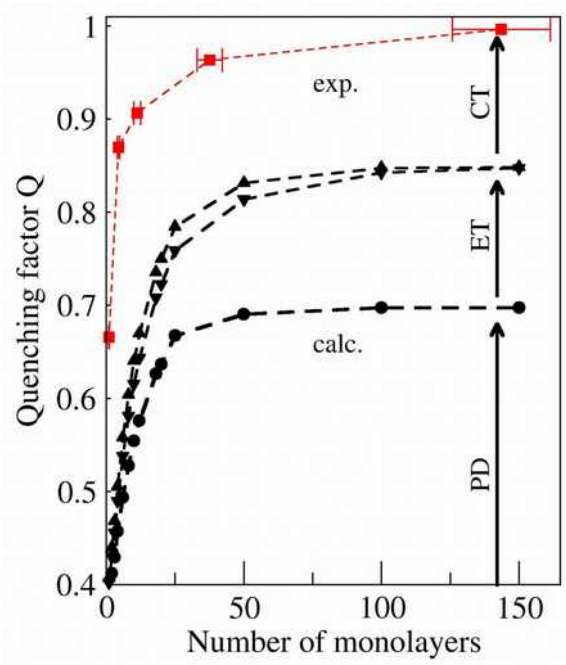

Figure 4: Quenching factor Q of the PL emission of the Au NPs as a function of the thickness (in monolayers) of the supporting $MoSe_2$ flake. The experimental values (red squares) are shown with error bars estimated assuming 10% relative uncertainty on the number of $MoSe_2$ monolayers. The contribution of solely plasmon damping (PD) to the calculated quenching factor is shown with black dots. The triangles show the calculated quenching factor when excitation transfer (ET) is taken into account in addition to the PD. Triangles up and down are obtained assuming the optical absorption of a monolayer $MoSe_2$ and bulk $MoSe_2$, respectively. The difference between measured PL quenching and calculated quenching is assigned to charge transfer (CT) quenching. Dashed lines are guides to the eye.

Obviously, the presence of the $MoSe_2$ layer strongly impacts the PL emission of the Au NPs which, to the best of our knowledge, was not reported up to now. This experimental finding has to be correlated with the quenchings of the PL emission and Raman scattering of monolayer $MoSe_2$ (Figure 2), and any explanation has to account for the PL quenching of both the monolayer $MoSe_2$ and of the Au NPs.

First, let's discuss how the optical properties of the Au NPs may be affected by the presence of the supporting $MoSe_2$ layer and in particular, to what extent the change in their optical absorption and emission rates can explain the quenching of their PL emission.

To address this point, we have performed electrodynamics simulations based on the discrete dipole approximation (DDA) method (Appendix) applied to a model system consisting of a hemispherical Au nanoparticle (17 nm in diameter corresponding to the average size revealed in Figure 1C) on top of a $MoSe_2$/ SiO_2 layer. Figure 5 displays electric near-field intensity maps generated at the laser excitation wavelength (532 nm) for an Au NP deposited on SiO_2 and on 1, 4 and 10 monolayers thick $MoSe_2$/ SiO_2. The numerical simulations clearly show that the electric near-field around and inside the nanoparticle is damped when the latter is supported by a $MoSe_2$ layer. The damping is more pronounced with increasing thickness of the $MoSe_2$ layer. It is due to the imaginary part of the complex dielectric function of $MoSe_2$, i.e., to the decay of the excited surface plasmons into electron-hole pairs (including excitons) in the MoSe2 layer. The electric near-field enhancement has been integrated over the Au

nanoparticle volume and the optical absorption of the laser energy by the nanoparticle has been estimated. The so-calculated optical absorption spectra point to plasmon damping indeed and to plasmonic-excitonic hybridization visible through absorption dips produced by the Fano-type interaction [4,5] between the red-shifted plasmonic resonance and the excitonic transitions (A and B) of the $MoSe_2$ layer (Figure A7A Appendix). Moreover, according to the calculations, the absorption of the laser light (producing the PL emission) of the Au NP is reduced by 39.2% in the case of Au NP on monolayer $MoSe_2$ compared to the situation where the nanoparticle is supported by SiO_2. Therefore, one expects that the PL emission of the Au NP on $MoSe_2$ is reduced by the same factor. Indeed, to take into account this plasmon damping effect, let's write the quenching factor as Eq.2:

$$Q = 1 - A(\lambda_{ex}, t) \qquad (2)$$

where A(λex, t) is the DDA-calculated optical absorption, at the laser excitation wavelength λex = 532 nm, of the Au NP on $MoSe_2$/ SiO_2, normalized to that of the same NP on SiO_2; As mentioned above Q depends on the thickness *t* of the $MoSe_2$ layer (Figures 5, A7).

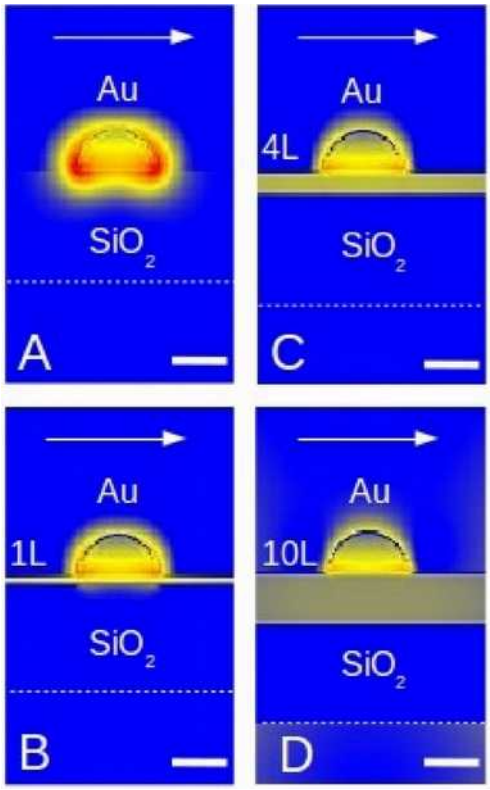

Figure 5: Electro-dynamics simulations, based on the discrete dipole approximation (DDA) method, of the optical electric field intensity enhancement |E|2/|E0|2 (E0 being the amplitude of the incident excitation field). The latter is displayed in log scale (red color corresponds to a factor 10 enhancement). Calculations were performed for the 532 nm laser wavelength used to excite the PL emission. The arrows indicate the polarization of the incident wave impinging a hemi-spherical Au nanoparticle (17 nm diameter) supported either directly by a 20 nm thick SiO_2 layer (A) or by a $MoSe_2$ layer with thickness of 1 (B), 4 (C) and 10 (D) monolayers. The lateral dimensions (130 x 130 nm²) were made sufficiently

large to minimize boundary surface effects. The dashed line shows the bottom of the SiO_2 layer. The horizontal bar is 10 nm long.

For Au NPs on monolayer $MoSe_2$, the calculated Plasmon Damping (PD) induced PL quenching factor is around 40% (Figure 4), a significant value which is however lower than the 66% observed experimentally. The calculated PD-induced quenching increases with increasing thickness of the $MoSe_2$ layer (Figures 5 and A7) and reaches a maximum value of 70 % for Au nanoparticle on a bulk-like $MoSe_2$ layer (150 monolayers, Figure 4). This value is still lower than the measured one (99.6%). It is worth to mention that the electron-hole pairs generated in the $MoSe_2$ layer by plasmon damping is submitted to charge transfer as well: the photogenerated electrons are transferred to the Au NPs and thus plasmon damping is not expected to increase the PL emission from the $MoSe_2$ layer.

Another possible reason for the quenching of the PL emission from the Au NPs could be the excitation transfer mechanism: the light emitted by radiative recombinations of electron-hole pairs localized into the Au NPs can be absorbed by the $MoSe_2$ layer, thus regenerating electron-hole pairs into the $MoSe_2$ layer. To account for this excitation transfer mechanism we assume that roughly half of the photons emitted by the Au NP is absorbed by the underlying $MoSe_2$ layer, whereas the other half is emitted towards the superior half-space and is collected by the microscope objective. In that case the quenching factor Q (Eq.2) becomes Eq.3.

$$Q = 1 - A\left(\lambda_{ex}, t\right)\frac{\left(1 - e^{-2\alpha(\lambda_{em})t}\right)}{2} \qquad (3)$$

Where $\alpha(\lambda_{em})$ is the absorption coefficient of the $MoSe_2$ layer at the emission wavelength λem of the Au NP. *As a first approximation, w*e assume that the path of the light emitted by the Au NP into the $MoSe_2$ layer is *2t* (t being the $MoSe_2$ layer thickness) in order to consider back reflection at the SiO_2 /Si interface. This of course leads to overestimation of optical absorption and excitation transfer in the case of $MoSe_2$ layer much thicker than the light penetration α-1. Figure 4 shows the quenching factor calculated according to Eq. 3 and using λ_{em} = 625 nm as the average PL emission wavelength of the Au NPs. Strictly speaking, because of the change of the electronic band structure induced by inter-layer Van der Walls interactions, the absorption coefficient α of a multi-layer $MoSe_2$ depends on its thickness *t*. For this reason, calculations of the ET contribution to the quenching factor were performed assuming the absorption coefficient of monolayer $MoSe_2$ [48] and of bulk $MoSe_2$ [49]. As can be noticed (Figure 4), whatever the absorption coefficient used in the calculations, the contribution of the excitation transfer mechanism to the quenching of the PL emission of the Au NPs is negligible in the case of few-layers $MoSe_2$ (up to 7 monolayers) because of their weak optical absorption. However, it increases with increasing layer thickness and reaches a maximum of 15% for bulk-like $MoSe_2$ (150 monolayers). As mentioned above, this value is certainly overestimated but it quantitatively indicates that the excitation transfer mechanism contributes significantly to the quenching of the Au NP PL emission in the case of bulk-like $MoSe_2$.

An additional reason for the reduced PL signal from the Au NPs on $MoSe_2$ layer could be the different interference effects experienced by the light emitted and reflected back at the SiO_2 /Si interface as the 90 nm SiO_2 layer forms a low-Q optical cavity. However, comparison of the calculated optical reflection properties of $MoSe_2$/ SiO_2 /Si and SiO_2 /Si stacks showed that, given the large numerical aperture of the collection objective and the unpolarized character of the PL emission from the Au NPs, such interference effects have only a weak impact (Figure A8 Appendix). Furthermore, the presence of Au NPs on the $MoSe_2$ layer surface does not lead to a decrease of the

optical absorption by the $MoSe_2$ layer, as shown by the DDA numerical simulations (Figure A7B Appendix). On the contrary, the optical absorption by the $MoSe_2$ layer is rather enhanced by the electric near-field produced by the hybrid plasmonic-excitonic resonances, particularly at the A and B exciton wavelengths (Figures A7B and C Appendix) in agreement with published works [50].

According to the difference between the measured quenching factor and the one calculated assuming PD + ET mechanisms (Figure 4) it appears that around 15% (in the case of thick $MoSe_2$) to 30% (in the case of few-layer $MoSe_2$) of the measured of quenching the PL emission of the Au NPs does not have an optical origin.

A possible source of quenching of the PL emission and Raman scattering observed for Au NPs deposited on $MoSe_2$ can be found in the electronic band alignment of the Au/ $MoSe_2$ system and in the CT phenomena taking place at the metal/semiconductor interface, which we now discuss.

.

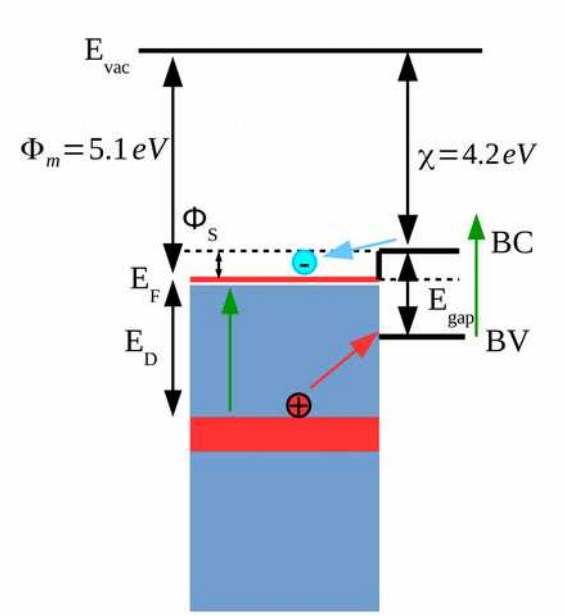

Figure 6: Energy level diagram of contacted a $MoSe_2$/Au Schottky interface. The arrows indicate the electrons and holes transfer between the $MoSe_2$ and Au. The green arrow represents the optical excitation energy (2.33 eV). Φ_m is the work function of Au, χ is the electron affinity of $MoSe_2$ and $\Phi_s = \Phi_m - \chi$ is the Schottky band offset at the $MoSe_2$/Au interface. BC and BV stand, respectively, for the conduction and valence band edges of $MoSe_2$. ED ~ 2.4 eV is the d-to-s bands transition energy edge in bulk Au.

According to photo-electron spectroscopy measurements, the electron affinity χ of $MoSe_2$ and the work function Φ_m of Au are respectively 4.2 and 5.1 eV [51,52]. Once the two materials are in contact, a Schottky junction with height $\Phi_s = \Phi_m - \chi$ is formed at the metal/semiconductor interface, in the absence of inter-mixing, impurities or defects which may pin the Fermi level. In the case of a thick $MoSe_2$ layer, the Φs = 0.9 eV band offset between the Fermi level of Au and the conduction band of $MoSe_2$ leads to band bending and to the formation of a barrier with height Φs, and a depletion layer which thickness is determined by the built-in potential V_{in} and the doping level of the

semiconductor

Typical depletion thicknesses W range from few nanometers, for heavily doped semiconductors, to few hundreds of micrometers for non-intentionally doped ones. In a thick semiconductor layer, the charge carriers are repelled away from the interface, but can possibly transfer to the metal by quantum tunnelling through the so-called Schottky barrier. In the case of monolayer $MoSe_2$/Au interface, the 2D semiconductor is much thinner (sub-nm thick) than the depletion layer. Hence, there is no depletion layer to consider in this case. Electrons in the conduction band of the monolayer $MoSe_2$ experience no Schottky barrier as shown in the band alignment diagram of Figure 6. They rather feel a Schottky well with depth Φs and can therefore readily transfer to the unoccupied states above the Fermi level of the Au NPs. In the case of electron-hole pairs generated by an optical excitation, the electrons in the conduction band of $MoSe_2$ are transferred to the Au NPs leaving behind the holes in the valence band. Electrons and holes are thus spatially separated, with almost no wavefunction overlapping which drops down the probability for radiative recombination and leads to a quenching of the PL emission of the monolayer $MoSe_2$ as observed experimentally (Figure 2A). This CT quenching mechanism has already been discussed in several published papers [10,21,25,26].

It is worth to mention that, in contrast with the PL quenching phenomenon discussed here, several studies reported, on the contrary, a rather strong enhancement of the PL from monolayer MoS_2 and $MoSe_2$ either transferred onto metal nanoparticles [5,50,53], using lift-off/transfer techniques [54], or supporting metal nanoparticles formed by e-beam lithography [55–57]. Because of the low operation temperature of these processes, it is unlikely that a Schottky metal/semiconductor interface is formed and hence no efficient CT from the TMD layer to the metal NP could take place. The interaction between the TMD layer and the metal nanoparticles is rather weak [58]. In that case, the strong plasmonic enhancement is responsible for increased PL emission from the TMD layer and may counterbalance a possible moderate PL quenching due to CT from the TMD layer to the metal NPs. In our samples, because the Au NPs grow on the $MoSe_2$ layer at high temperature, it is likely that hybridization of electronic states at the $MoSe_2$/Au interface occurs thus leading to the formation of a Schottky interface [59–61]. Therefore, electrons may efficiently transfer from the $MoSe_2$ layer to the Au NPs, which is responsible for the quenching of the PL emission of $MoSe_2$. In addition, the latter cannot be counterbalanced by any plasmonic enhancement because of the large broadening of the SP resonance in our Au NPs (Figures A2-A7 Appendix).

Let’s comment on the fact that the PL emission of the $MoSe_2$ layer is totally quenched in the samples deposited with 4.8 and 0.8 nm equivalent thicknesses, under high optical pumping at liquid nitrogen temperature (Figure A1). As a matter of fact, the decay time of the PL emission measured in monolayer $MoSe_2$ is of the order of 1 nanosecond [62] at room temperature. We here suggest that the transfer of the photo-excited electrons from the $MoSe_2$ layer to the Au NPs is much faster; under this condition, the formation and recombination of excitons becomes highly unlikely thus leading to strong quenching of the PL emission from the $MoSe_2$ layer.

Moreover, the quenching of the Raman scattering by $MoSe_2$ phonons observed for $MoSe_2$ layers covered with Au NPs (Figures A4 and A6 Appendix), gives an additional indication for an even faster (than 1 nanosecond time scale) electron transfer. Indeed, Shree et al [63] have investigated the temperature dependence of the exciton linewidth in monolayer $MoSe_2$ and have estimated the exciton-phonon scattering time. Using the acoustic and optical exciton-phonon coupling strengths reported in ref [63], we found that the exciton-phonon scattering time is in the 15-20

femtoseconds (fs) range, at room temperature. Hence, providing that the electron transfer time from the $MoSe_2$ layer to the Au NPs is smaller than 15-20 fs, the photo-excited electron could leave the $MoSe_2$ layer before it emits a phonon. In other words, the electron transfer may quench the exciton-phonon interaction, thus leading to a lower Raman efficiency (Figures A4 and A6) and to a total quenching of the PL emission in $MoSe_2$ layer covered with Au NPs compared to bare $MoSe_2$ (Figures 2 and 3).

We now focus on the quenching of the PL emission of the Au NPs not explained by the PD and ET mechanisms.

As shown in the energy diagram of Figure 4, gold has an optical absorption band edge around Ed ~ 2.4 eV due to transitions of electrons from the d-band to the unoccupied states of the s-band above the Fermi level [64]. The d-band is characterized by a large bandwidth due to the density of states associated with the dispersion curves in the different directions of the Brillouin zone. The optical excitation energy used in our experiments (532 nm, i.e., 2.33 eV) is nearly resonant with the d-s transition, and, as mentioned above, the electron-hole pairs photo-generated in the Au NPs may recombine radiatively giving rise to the broad PL emission observed in Figures 2B and 3B. Because of the electron transfer from the monolayer $MoSe_2$ to the Au NPs discussed above, one would expect an enhancement, rather than a quenching, of the PL emission from the Au NPs grown on $MoSe_2$. Indeed, since the $MoSe_2$ layer acts as an electron source, the electron density in the Au NPs should increase and so the probability of their radiative recombination with the holes photo-generated in the d-band of the Au NPs. This is however opposite to the experimental findings (Figures 2, 3) which indicate a partial quenching of the PL emission of the Au NPs grown on $MoSe_2$ layer.

The energy diagram in Figure 6 shows that the d-band of Au is at a lower energy than the valence band of $MoSe_2$. The $MoSe_2$/Au valence band offset is $\Delta Ev,d = \Phi s + (Ed - Egap)$; Egap being the band gap energy of the $MoSe_2$ layer. Using the values quoted in Figure 6, one obtains $\Delta Ev,d \approx 1.9$ eV. This large valence band offset constitutes a deep well for the holes photo-generated in the d-band of the Au NP. It is thus energetically favorable for such a hole to transfer to the valence band of $MoSe_2$, i.e., for an electron in the valence band of $MoSe_2$ to transfer to a free d-electron state of the Au NP. Consequently, the probability for electrons at the Fermi level of the Au NP to recombine radiatively is decreased due to the leakage of the photo-generated holes from the Au NP to the $MoSe_2$ layer. This second CT pathway of holes from the Au NPs to the $MoSe_2$ layer is here introduced as a possible origin of the difference between the measured overall quenching of the PL emission of the Au NP and the one calculated by considering both PD and ET contributions. To complement Eq 3., the quenching factor can be now expressed as

$$Q = 1 - A(\lambda_{ex}, t)\frac{\left(1 - e^{-2\alpha(\lambda_{em})t}\right)}{2}\eta_{CT}(t) \qquad (4)$$

Where $\eta_{CT}(t)$ accounts for the contribution of the CT mechanism to the quenching of the PL emission of the Au NPs. It depends on the thickness t of the $MoSe_2$ layer as shown in Figure 4: it contributes for around 30% to the overall quenching in the case of monolayer $MoSe_2$ and 15% in the case of bulk-like $MoSe_2$.

Unlike the one observed for the $MoSe_2$ layer (Figure 2A), the quenching of the PL emission of the Au NPs is not total (Figure 2B). We suggest that this difference lies in the different temporal dynamics of the PL emission of the $MoSe_2$ layer and of the Au NPs. Indeed, because there is a large density of electrons below the Fermi level in the

metallic NP, the electrons recombine radiatively with the photo-generated holes and emit light on a sub-picosecond time scale [65] in agreement with the large spectral width of the PL emission (Figure 3B). Therefore, electron-hole pairs photo-excited in an Au NP may partly recombine radiatively before the holes escape to the $MoSe_2$ layer. In other words, the transfer of holes from the Au NPs to the $MoSe_2$ and the radiative recombination of electron-hole pairs within the Au NPs may occur on the same time scale and counterbalance each other, leading thus to only a partial PL quenching. Finally, Figures 3 and 4 clearly show that the measured quenching of the PL emission from the Au NPs increases towards its maximum value (Q=1) with increasing thickness of the $MoSe_2$ layer. This behavior is well accounted for by the calculated PD and ET quenching mechanisms (Figure 4). It also indicates that the CT mechanism contributes to the total quenching by an additional 30% in the case of few-layers $MoSe_2$ (up to 7 monolayers) a value which decreases to around 15% in the case of bulk-like $MoSe_2$ layer (Figure 4). The fact that the CT rate is slowed down with increasing $MoSe_2$ layer thickness can be understood in terms of Schottky barrier and depletion zone formation at the bulk-like $MoSe_2$/Au interface which may prevent the photo-generated holes to escape from the Au NPs to the $MoSe_2$ layer.-

Conclusions

We have investigated the optical properties of hybrid $MoSe_2$/Au nanostructures formed by sputtering of gold nanoparticles on CVD grown single- and multilayer $MoSe_2$. We reported the observation of a complete quenching of the photoluminescence emission of monolayer $MoSe_2$. We have verified that this complete quenching was not due to the strain caused by the growth of Au on $MoSe_2$, nor to excitation transfer due to optical absorption by the Au NPs. It is interpreted in terms of electron transfer from the monolayer $MoSe_2$ to the Au NPs, which corroborates previously reported results and interpretations. In addition, we have exploited the photoluminescence emission of the Au NPs deposited on the $MoSe_2$ layer. Using spatially resolved photoluminescence, a partial quenching of the PL emission of the Au NPs was pointed out and measured as a function of the $MoSe_2$ flake thickness. These results are explained by i) Plasmon damping and subsequent reduced optical absorption of the laser light by the Au NPs which can be understood in terms of surface plasmons decay into electron-hole pair excitations of the $MoSe_2$ layer, ii) An excitation transfer mechanism in which the photon emitted by radiative recombinations of electron-hole pairs localized into the Au NPs is absorbed by the $MoSe_2$ layer and converted into an electron-hole pair into the TMD sheet iii) Charge transfer of the holes photo-generated in the Au NPs due to the band alignment diagram at the semiconductor/metal interface which allows the holes in the Au NPs to leak towards the $MoSe_2$ layer. The plasmon damping, the energy transfer mechanisms and the two-pathways CT mechanism of electrons from the $MoSe_2$ layer to the Au NPs, and vice versa of holes from the Au NPs to the $MoSe_2$ layer, explain well the quenching of the photoluminescence of both the $MoSe_2$ layers and the Au nanoparticles when they are put in contact and form a Schottky junction. This work complements the interpretations proposed in the literature and contributes to the understanding of the complex properties of the metal/TMD interface. Moreover, the presented results may be useful for applications in highly sensitive photo-detectors since radiative losses are eliminated by PL quenching and CT to high mobility materials may improve the overall performances of nano-optical devices.

Acknowledgements

This work was granted access to the HPC resources of CALMIP supercomputing center under the allocation 2020-P0996. The work has been supported by the EUR grant NanoX n° ANR-17-EURE-0009 in the framework of the “Programme des Investissements d’Avenir"

Data availability

The raw/processed data required to reproduce these findings cannot be shared at this time due to technical or time limitations.

References

[1] J. Cuadra, D.G. Baranov, M. Wersäll, R. Verre, T.J. Antosiewicz, T. Shegai, Observation of Tunable Charged Exciton Polaritons in Hybrid Monolayer WS2−Plasmonic Nanoantenna System, Nano Lett. 18 (2018) 1777–1785. https://doi.org/10.1021/acs.nanolett.7b04965.

[2] B. Lee, J. Park, G.H. Han, H.-S. Ee, C.H. Naylor, W. Liu, A.T.C. Johnson, R. Agarwal, Fano Resonance and Spectrally Modified Photoluminescence Enhancement in Monolayer MoS2 Integrated with Plasmonic Nanoantenna Array, Nano Lett. 15 (2015) 3646–3653. https://doi.org/10.1021/acs.nanolett.5b01563.

[3] W. Liu, B. Lee, C.H. Naylor, H.-S. Ee, J. Park, A.T.C. Johnson, R. Agarwal, Strong Exciton–Plasmon Coupling in MoS2 Coupled with Plasmonic Lattice, Nano Lett. 16 (2016) 1262–1269. https://doi.org/10.1021/acs.nanolett.5b04588.

[4] I. Abid, A. Bohloul, S. Najmaei, C. Avendano, H.-L. Liu, R. Péchou, A. Mlayah, J. Lou, Resonant surface plasmon–exciton interaction in hybrid $MoSe_2$@Au nanostructures, Nanoscale. 8 (2016) 8151–8159. https://doi.org/10.1039/C6NR00829A.

[5] I. Abid, W. Chen, J. Yuan, A. Bohloul, S. Najmaei, C. Avendano, R. Péchou, A. Mlayah, J. Lou, Temperature-Dependent Plasmon–Exciton Interactions in Hybrid Au/$MoSe_2$ Nanostructures, ACS Photonics. 4 (2017) 1653–1660. https://doi.org/10.1021/acsphotonics.6b00957.

[6] A. Sobhani, A. Lauchner, S. Najmaei, C. Ayala-Orozco, F. Wen, J. Lou, N.J. Halas, Enhancing the photocurrent and photoluminescence of single crystal monolayer MoS2 with resonant plasmonic nanoshells, Appl. Phys. Lett. 104 (2014) 031112. https://doi.org/10.1063/1.4862745.

[7] J. Li, Q. Ji, S. Chu, Y. Zhang, Y. Li, Q. Gong, K. Liu, K. Shi, Tuning the photo-response in monolayer MoS2 by plasmonic nano-antenna, Scientific Reports. 6 (2016) 23626. https://doi.org/10.1038/srep23626.

[8] J. Miao, W. Hu, Y. Jing, W. Luo, L. Liao, A. Pan, S. Wu, J. Cheng, X. Chen, W. Lu, Surface Plasmon-Enhanced Photodetection in Few Layer MoS2 Phototransistors with Au Nanostructure Arrays, Small. 11 (2015) 2392–2398. https://doi.org/10.1002/smll.201403422.

[9] X. Yang, W. Liu, M. Xiong, Y. Zhang, T. Liang, J. Yang, M. Xu, J. Ye, H. Chen, Au nanoparticles on ultrathin MoS_2 sheets for plasmonic organic solar cells, Journal of Materials Chemistry A. 2 (2014) 14798. https://doi.org/10.1039/C4TA03178D.

[10] K. Abid, N.H. Belkhir, S.B. Jaber, R. Zribi, M.G. Donato, G. Di Marco, P.G. Gucciardi, G. Neri, R. Maâlej, Photoinduced Enhanced Raman Spectroscopy with Hybrid Au@WS_2 Nanosheets, J. Phys. Chem. C. 124 (2020) 20350–20358. https://doi.org/10.1021/acs.jpcc.0c04664.

[11] B.L. Li, J. Wang, H.L. Zou, S. Garaj, C.T. Lim, J. Xie, N.B. Li, D.T. Leong, Low-Dimensional Transition Metal Dichalcogenide Nanostructures Based Sensors, Advanced Functional Materials. 26 (2016) 7034–7056. https://doi.org/10.1002/adfm.201602136.
[12] Z. Zhu, J. Yuan, H. Zhou, J. Hu, J. Zhang, C. Wei, F. Yu, S. Chen, Y. Lan, Y. Yang, Y. Wang, C. Niu, Z. Ren, J. Lou, Z. Wang, J. Bao, Excitonic Resonant Emission–Absorption of Surface Plasmons in Transition Metal Dichalcogenides for Chip-Level Electronic–Photonic Integrated Circuits, ACS Photonics. 3 (2016) 869–874. https://doi.org/10.1021/acsphotonics.6b00101.
[13] Z. Yin, B. Chen, M. Bosman, X. Cao, J. Chen, B. Zheng, H. Zhang, Au Nanoparticle-Modified MoS_2 Nanosheet-Based Photoelectrochemical Cells for Water Splitting, Small. 10 (2014) 3537–3543. https://doi.org/10.1002/smll.201400124.
[14] Z. Li, Y. Xiao, Y. Gong, Z. Wang, Y. Kang, S. Zu, P.M. Ajayan, P. Nordlander, Z. Fang, Active Light Control of the MoS_2 Monolayer Exciton Binding Energy, ACS Nano. 9 (2015) 10158–10164. https://doi.org/10.1021/acsnano.5b03764.
[15] R. Jiang, B. Li, C. Fang, J. Wang, Metal/Semiconductor Hybrid Nanostructures for Plasmon-Enhanced Applications, Adv. Mater. 26 (2014) 5274–5309. https://doi.org/10.1002/adma.201400203.
[16] C. Gong, C. Huang, J. Miller, L. Cheng, Y. Hao, D. Cobden, J. Kim, R.S. Ruoff, R.M. Wallace, K. Cho, X. Xu, Y.J. Chabal, Metal Contacts on Physical Vapor Deposited Monolayer MoS_2, ACS Nano. 7 (2013) 11350–11357. https://doi.org/10.1021/nn4052138.
[17] D. Zhang, Y.-C. Wu, M. Yang, X. Liu, C.Ó. Coileáin, H. Xu, M. Abid, M. Abid, J.-J. Wang, I.V. Shvets, H. Liu, Z. Wang, H. Yin, H. Liu, B.S. Chun, X. Zhang, H.-C. Wu, Probing thermal expansion coefficients of monolayers using surface enhanced Raman scattering, RSC Adv. 6 (2016) 99053–99059. https://doi.org/10.1039/C6RA20623A.
[18] D. Zhang, Y.-C. Wu, M. Yang, X. Liu, C.Ó. Coileáin, M. Abid, M. Abid, J.-J. Wang, I. Shvets, H. Xu, B.S. Chun, H. Liu, H.-C. Wu, Surface enhanced Raman scattering of monolayer MX2 with metallic nano particles, Scientific Reports. 6 (2016) 30320. https://doi.org/10.1038/srep30320.
[19] Y. Deng, M. Chen, J. Zhang, Z. Wang, W. Huang, Y. Zhao, J.P. Nshimiyimana, X. Hu, X. Chi, G. Hou, X. Zhang, Y. Guo, L. Sun, Thickness-dependent morphologies of Ag on n-layer MoS2 and its surface-enhanced Raman scattering, Nano Research. 9 (2016) 1682–1688. https://doi.org/10.1007/s12274-016-1062-5.
[20] S. Shankar Singha, D. Nandi, A. Singha, Tuning the photoluminescence and ultrasensitive trace detection properties of few-layer MoS 2 by decoration with gold nanoparticles, RSC Advances. 5 (2015) 24188–24193. https://doi.org/10.1039/C5RA01439E.
[21] U. Bhanu, M.R. Islam, L. Tetard, S.I. Khondaker, Photoluminescence quenching in gold - MoS2 hybrid nanoflakes, Scientific Reports. 4 (2014). https://doi.org/10.1038/srep05575.
[22] Y. Sun, K. Liu, X. Hong, M. Chen, J. Kim, S. Shi, J. Wu, A. Zettl, F. Wang, Probing Local Strain at MX_2 –Metal Boundaries with Surface Plasmon-Enhanced Raman Scattering, Nano Letters. 14 (2014) 5329–5334. https://doi.org/10.1021/nl5023767.
[23] N. Kang, H.P. Paudel, M.N. Leuenberger, L. Tetard, S.I. Khondaker, Photoluminescence Quenching in Single-Layer MoS_2 via Oxygen Plasma Treatment, The Journal of Physical Chemistry C. 118 (2014) 21258–21263. https://doi.org/10.1021/jp506964m.
[24] J. Yuan, S. Najmaei, Z. Zhang, J. Zhang, S. Lei, P. M. Ajayan, B.I. Yakobson, J. Lou, Photoluminescence Quenching and Charge Transfer in Artificial Heterostacks of Monolayer Transition Metal Dichalcogenides and Few-Layer Black Phosphorus, ACS Nano. 9 (2015) 555–563. https://doi.org/10.1021/nn505809d.

[25] S.Y. Kim, H.I. Yang, W. Choi, Photoluminescence quenching in monolayer transition metal dichalcogenides by Al2O3 encapsulation, Appl. Phys. Lett. (2018) 6.
[26] L. Zhang, H. Yan, X. Sun, M. Dong, T. Yildirim, B. Wang, B. Wen, G.P. Neupane, A. Sharma, Y. Zhu, J. Zhang, K. Liang, B. Liu, H.T. Nguyen, D. Macdonald, Y. Lu, Modulated interlayer charge transfer dynamics in a monolayer TMD/metal junction, Nanoscale. 11 (2019) 418–425. https://doi.org/10.1039/C8NR08728H.
[27] P. Tonndorf, R. Schmidt, P. Böttger, X. Zhang, J. Börner, A. Liebig, M. Albrecht, C. Kloc, O. Gordan, D.R. Zahn, others, Photoluminescence emission and Raman response of monolayer MoS 2, MoSe 2, and WSe 2, Optics Express. 21 (2013) 4908–4916.
[28] Y. Zhang, T.-R. Chang, B. Zhou, Y.-T. Cui, H. Yan, Z. Liu, F. Schmitt, J. Lee, R. Moore, Y. Chen, H. Lin, H.-T. Jeng, S.-K. Mo, Z. Hussain, A. Bansil, Z.-X. Shen, Direct observation of the transition from indirect to direct bandgap in atomically thin epitaxial MoSe2, Nat Nano. 9 (2014) 111–115. https://doi.org/10.1038/nnano.2013.277.
[29] J. Xia, X. Huang, L.-Z. Liu, M. Wang, L. Wang, B. Huang, D.-D. Zhu, J.-J. Li, C.-Z. Gu, X.-M. Meng, CVD synthesis of large-area, highly crystalline MoSe 2 atomic layers on diverse substrates and application to photodetectors, Nanoscale. 6 (2014) 8949–8955. https://doi.org/10.1039/C4NR02311K.
[30] J.C. Shaw, H. Zhou, Y. Chen, N.O. Weiss, Y. Liu, Y. Huang, X. Duan, Chemical vapor deposition growth of monolayer MoSe2 nanosheets, Nano Res. 7 (2015) 511–517. https://doi.org/10.1007/s12274-014-0417-z.
[31] G. Honjo, K. Takayanagi, K. Kobayashi, K. Yagi, On cluster mobilities in nucleation and growth processes of epitaxial thin films, Physica Status Solidi (a). 55 (1979) 353–367. https://doi.org/10.1002/pssa.2210550203.
[32] C. Maurel, F. Ajustron, R. Péchou, G. Seine, R. Coratger, Electrical behavior of the Au/MoS2 interface studied by light emission induced by scanning tunneling microscopy, Surface Science. 600 (2006) 442–447. https://doi.org/10.1016/j.susc.2005.10.042.
[33] A. Carladous, R. Coratger, F. Ajustron, G. Seine, R. Péchou, J. Beauvillain, Light emission from spectral analysis of Au/MoS_2 nanocontacts stimulated by scanning tunneling microscopy, Phys. Rev. B. 66 (2002) 045401. https://doi.org/10.1103/PhysRevB.66.045401.
[34] T.P. Darby, C.M. Wayman, Growth of gold films on air- and vacuum-cleaved molybdenite, Physica Status Solidi (a). 25 (1974) 585–590. https://doi.org/10.1002/pssa.2210250227.
[35] H. Chen, X. Kou, Z. Yang, W. Ni, J. Wang, Shape- and Size-Dependent Refractive Index Sensitivity of Gold Nanoparticles, Langmuir. 24 (2008) 5233–5237. https://doi.org/10.1021/la800305j.
[36] X. Zhang, X.-F. Qiao, W. Shi, J.-B. Wu, D.-S. Jiang, P.-H. Tan, Phonon and Raman scattering of two-dimensional transition metal dichalcogenides from monolayer, multilayer to bulk material, Chem. Soc. Rev. 44 (2015) 2757–2785. https://doi.org/10.1039/C4CS00282B.
[37] S. Horzum, H. Sahin, S. Cahangirov, P. Cudazzo, A. Rubio, T. Serin, F.M. Peeters, Phonon softening and direct to indirect band gap crossover in strained single-layer MoSe 2, Physical Review B. 87 (2013). https://doi.org/10.1103/PhysRevB.87.125415.
[38] J.O. Island, A. Kuc, E.H. Diependaal, R. Bratschitsch, H.S. van der Zant, T. Heine, A. Castellanos-Gomez, Precise and reversible band gap tuning in single-layer MoSe 2 by uniaxial strain, Nanoscale. 8 (2016) 2589–2593.
[39] C.R. Zhu, G. Wang, B.L. Liu, X. Marie, X.F. Qiao, X. Zhang, X.X. Wu, H. Fan, P.H. Tan, T. Amand, B. Urbaszek, Strain tuning of optical emission energy and polarization in monolayer and bilayer MoS 2, Physical Review B. 88 (2013). https://doi.org/10.1103/PhysRevB.88.121301.

[40] Y. Wang, C. Cong, W. Yang, J. Shang, N. Peimyoo, Y. Chen, J. Kang, J. Wang, W. Huang, T. Yu, Strain-induced direct–indirect bandgap transition and phonon modulation in monolayer WS2, Nano Research. 8 (2015) 2562–2572. https://doi.org/10.1007/s12274-015-0762-6.

[41] A. Morales-Garcia, E. del Corro, M. Kalbac, O. Frank, Tuning the electronic properties of monolayer and bilayer transition metal dichalcogenide compounds under direct out-of-plane compression, Phys. Chem. Chem. Phys. (2017). https://doi.org/10.1039/C7CP00012J.

[42] H.J. Conley, B. Wang, J.I. Ziegler, R.F. Haglund, S.T. Pantelides, K.I. Bolotin, Bandgap Engineering of Strained Monolayer and Bilayer MoS_2, Nano Letters. 13 (2013) 3626–3630. https://doi.org/10.1021/nl4014748.

[43] K. He, C. Poole, K.F. Mak, J. Shan, Experimental Demonstration of Continuous Electronic Structure Tuning via Strain in Atomically Thin MoS_2, Nano Letters. 13 (2013) 2931–2936. https://doi.org/10.1021/nl4013166.

[44] L. Sortino, M. Brooks, P.G. Zotev, A. Genco, J. Cambiasso, S. Mignuzzi, S.A. Maier, G. Burkard, R. Sapienza, A.I. Tartakovskii, Dielectric Nanoantennas for Strain Engineering in Atomically Thin Two-Dimensional Semiconductors, ACS Photonics. 7 (2020) 2413–2422. https://doi.org/10.1021/acsphotonics.0c00294.

[45] P.G. Etchegoin, E.C. Le Ru, M. Meyer, An analytic model for the optical properties of gold, The Journal of Chemical Physics. 125 (2006) 164705. https://doi.org/10.1063/1.2360270.

[46] J. Zheng, C. Zhou, M. Yu, J. Liu, Different sized luminescent gold nanoparticles, Nanoscale. 4 (2012) 4073. https://doi.org/10.1039/c2nr31192e.

[47] T. Zhang, G. Lu, H. Shen, K. Shi, Y. Jiang, D. Xu, Q. Gong, Photoluminescence of a single complex plasmonic nanoparticle, Scientific Reports. 4 (2014). https://doi.org/10.1038/srep03867.

[48] H.-L. Liu, C.-C. Shen, S.-H. Su, C.-L. Hsu, M.-Y. Li, L.-J. Li, Optical properties of monolayer transition metal dichalcogenides probed by spectroscopic ellipsometry, Appl. Phys. Lett. 105 (2014) 201905. https://doi.org/10.1063/1.4901836.

[49] Y. Niu, S. Gonzalez-Abad, R. Frisenda, P. Marauhn, M. Drüppel, P. Gant, R. Schmidt, N. Taghavi, D. Barcons, A. Molina-Mendoza, S. de Vasconcellos, R. Bratschitsch, D. Perez De Lara, M. Rohlfing, A. Castellanos-Gomez, Thickness-Dependent Differential Reflectance Spectra of Monolayer and Few-Layer MoS2, MoSe2, WS2 and WSe2, Nanomaterials. 8 (2018) 725. https://doi.org/10.3390/nano8090725.

[50] S. Najmaei, A. Mlayah, A. Arbouet, C. Girard, J. Léotin, J. Lou, Plasmonic Pumping of Excitonic Photoluminescence in Hybrid MoS_2–Au Nanostructures, ACS Nano. 8 (2014) 12682–12689. https://doi.org/10.1021/nn5056942.

[51] J. Kang, S. Tongay, J. Zhou, J. Li, J. Wu, Band offsets and heterostructures of two-dimensional semiconductors, Applied Physics Letters. 102 (2013) 012111.

[52] Y.-H. Chang, W. Zhang, Y. Zhu, Y. Han, J. Pu, J.-K. Chang, W.-T. Hsu, J.-K. Huang, C.-L. Hsu, M.-H. Chiu, T. Takenobu, H. Li, C.-I. Wu, W.-H. Chang, A.T.S. Wee, L.-J. Li, Monolayer $MoSe_2$ Grown by Chemical Vapor Deposition for Fast Photodetection, ACS Nano. 8 (2014) 8582–8590. https://doi.org/10.1021/nn503287m.

[53] H. Chen, J. Yang, E. Rusak, J. Straubel, R. Guo, Y.W. Myint, J. Pei, M. Decker, I. Staude, C. Rockstuhl, Y. Lu, Y.S. Kivshar, D. Neshev, Manipulation of photoluminescence of two-dimensional $MoSe_2$ by gold nanoantennas, Scientific Reports. 6 (2016) srep22296. https://doi.org/10.1038/srep22296.

[54] X. Wang, K. Kang, S. Chen, R. Du, E.-H. Yang, Location-specific growth and transfer of arrayed MoS 2 monolayers with controllable size, 2D Mater. 4 (2017) 025093. https://doi.org/10.1088/2053-1583/aa6e69.
[55] S. Butun, S. Tongay, K. Aydin, Enhanced Light Emission from Large-Area Monolayer MoS2 Using Plasmonic Nanodisc Arrays, Nano Lett. 15 (2015) 2700–2704. https://doi.org/10.1021/acs.nanolett.5b00407.
[56] E. Palacios, S. Park, S. Butun, L. Lauhon, K. Aydin, Enhanced radiative emission from monolayer MoS2 films using a single plasmonic dimer nanoantenna, Appl. Phys. Lett. 111 (2017) 031101. https://doi.org/10.1063/1.4993427.
[57] B. Lee, J. Park, G.H. Han, H.-S. Ee, C.H. Naylor, W. Liu, A.T.C. Johnson, R. Agarwal, Fano Resonance and Spectrally Modified Photoluminescence Enhancement in Monolayer MoS2 Integrated with Plasmonic Nanoantenna Array, Nano Lett. 15 (2015) 3646–3653. https://doi.org/10.1021/acs.nanolett.5b01563.
[58] M. Alamri, R. Sakidja, R. Goul, S. Ghopry, J.Z. Wu, Plasmonic Au Nanoparticles on 2D MoS_2 /Graphene van der Waals Heterostructures for High-Sensitivity Surface-Enhanced Raman Spectroscopy, ACS Appl. Nano Mater. 2 (2019) 1412–1420. https://doi.org/10.1021/acsanm.8b02308.
[59] L. Huang, B. Li, M. Zhong, Z. Wei, J. Li, Tunable Schottky Barrier at $MoSe_2$ /Metal Interfaces with a Buffer Layer, J. Phys. Chem. C. 121 (2017) 9305–9311. https://doi.org/10.1021/acs.jpcc.7b00383.
[60] C. Gong, L. Colombo, R.M. Wallace, K. Cho, The Unusual Mechanism of Partial Fermi Level Pinning at Metal–MoS_2 Interfaces, Nano Lett. 14 (2014) 1714–1720. https://doi.org/10.1021/nl403465v.
[61] I. Popov, G. Seifert, D. Tománek, Designing Electrical Contacts to MoS 2 Monolayers: A Computational Study, Phys. Rev. Lett. 108 (2012) 156802. https://doi.org/10.1103/PhysRevLett.108.156802.
[62] C. Robert, D. Lagarde, F. Cadiz, G. Wang, B. Lassagne, T. Amand, A. Balocchi, P. Renucci, S. Tongay, B. Urbaszek, X. Marie, Exciton radiative lifetime in transition metal dichalcogenide monolayers, Phys. Rev. B. 93 (2016) 205423. https://doi.org/10.1103/PhysRevB.93.205423.
[63] S. Shree, M. Semina, C. Robert, B. Han, T. Amand, A. Balocchi, M. Manca, E. Courtade, X. Marie, T. Taniguchi, K. Watanabe, M.M. Glazov, B. Urbaszek, Observation of exciton-phonon coupling in MoSe 2 monolayers, Phys. Rev. B. 98 (2018) 035302. https://doi.org/10.1103/PhysRevB.98.035302.
[64] P.B. Johnson, R.W. Christy, Optical Constants of the Noble Metals, Phys. Rev. B. 6 (1972) 4370–4379. https://doi.org/10.1103/PhysRevB.6.4370.
[65] E. Sakat, I. Bargigia, M. Celebrano, A. Cattoni, S. Collin, D. Brida, M. Finazzi, C. D'Andrea, P. Biagioni, Time-Resolved Photoluminescence in Gold Nanoantennas, ACS Photonics. 3 (2016) 1489–1493. https://doi.org/10.1021/acsphotonics.6b00039.

Plasmon damping and charge transfer pathways in Au@$MoSe_2$ nanostructures

Appendix

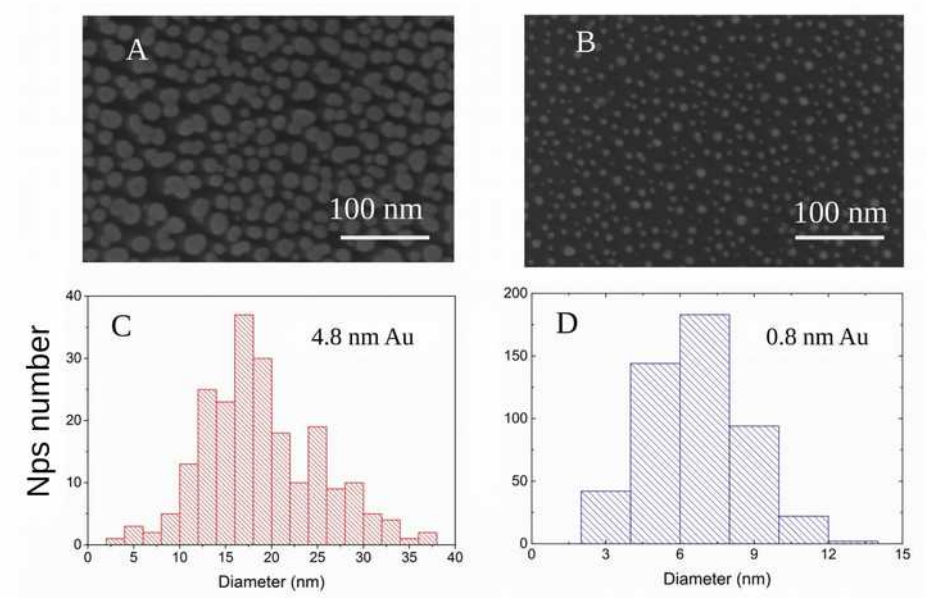

Figure A1: A,B) Scanning Electron Microscopy images of Au NPs sputtered on SiO_2/Si substrate. The equivalent thicknesses of a 2D Au layer with the same volume are 4.8nm in A and 0.8nm in B. C, D) NPs size distribution histograms obtained from the SEM images. The Au NPs average size is 17 nm in C and 7 nm in D [1].

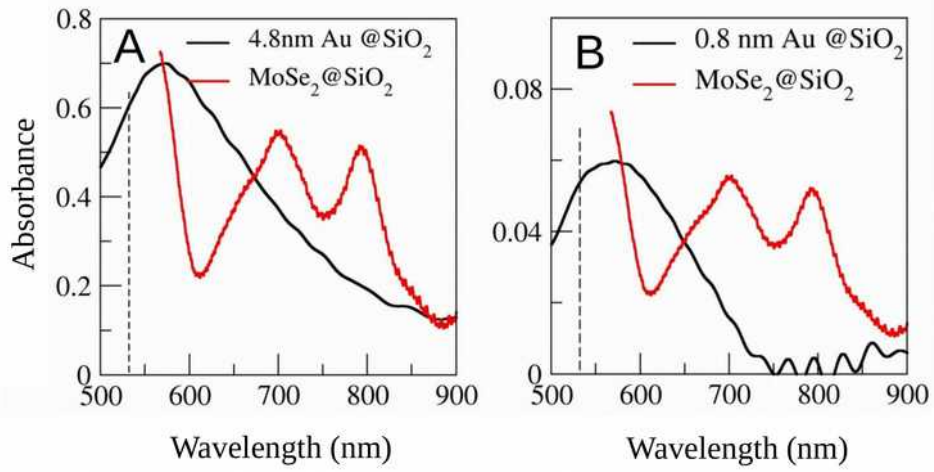

Figure A2: Absorbance spectra of Au nanoparticles deposited on SiO_2 (black) for 4.8 (A) and 0.8 nm (B) deposited equivalent thicknesses and of bare monolayer $MoSe_2$ grown by CVD on SiO_2 substrate (red). The absorbance spectrum of Au NPs on SiO_2 is much weaker in B compared to A because of the much lower Au NPs density and size (see Figure A1). The spectrum of $MoSe_2/SiO_2$ is the same in A and B and has been rescaled for comparison with the absorption spectrum of the Au NPs. The vertical dashed line shows the laser excitation wavelength 532 nm used to excite the photoluminescence emission.

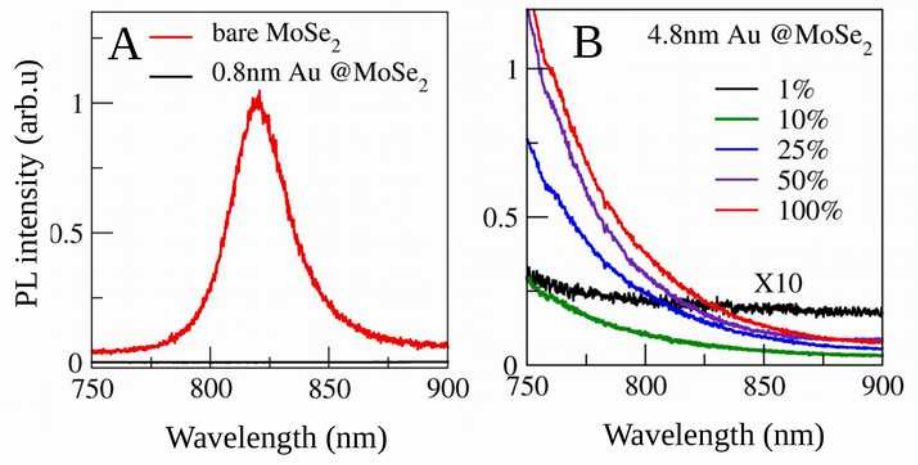

Figure A3: A) Room temperature photoluminescence spectra of bare $MoSe_2$ (red) and $MoSe_2$ covered with Au NPs (0.8 nm equivalent thickness) (black) excited with 532 nm laser wavelength. B) Liquid Nitrogen temperature photoluminescence spectra of $MoSe_2$ covered with Au NPs (4.8 nm equivalent thickness) excited at 532 nm laser wavelength with laser intensity increasing from 1% to 100% of the maximum value 10^6 W/cm ^{2}. The increase of the detected signal, with increasing laser intensity, is due to the long-wavelengths tail of the PL emission of the Au NPs. The PL emission of the $MoSe_2$ layer is totally quenched.

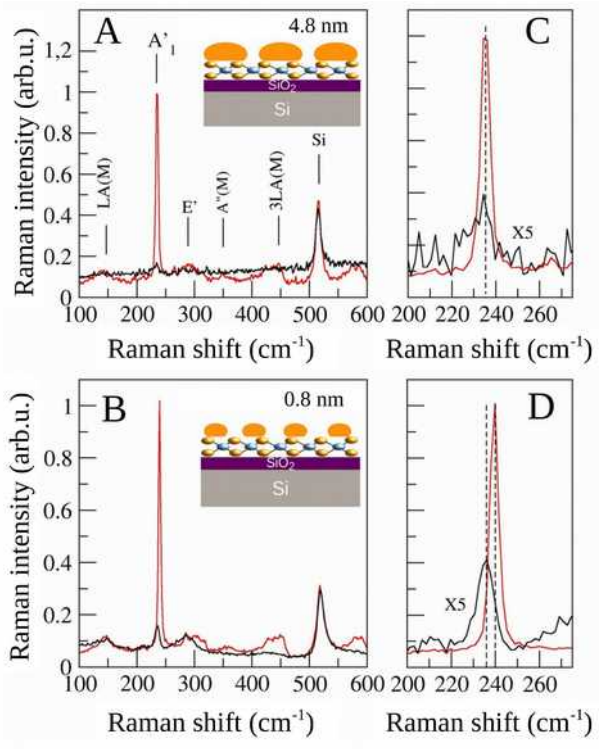

Figure A4: Raman scattering spectra of bare monolayer $MoSe_2$ (red) and of Au NPs-covered monolayer $MoSe_2$ (black) for (A, C) 4.8 nm and (B, D) 0.8 nm deposited equivalent thicknesses. (C) and (D) show the 200-270 cm^{-1} spectral region of Figures A and B, centered on the A'_1 phonon wavenumber. The spectra of $MoSe_2$ covered with Au NPs are multiplied by a factor 5 in C and D.

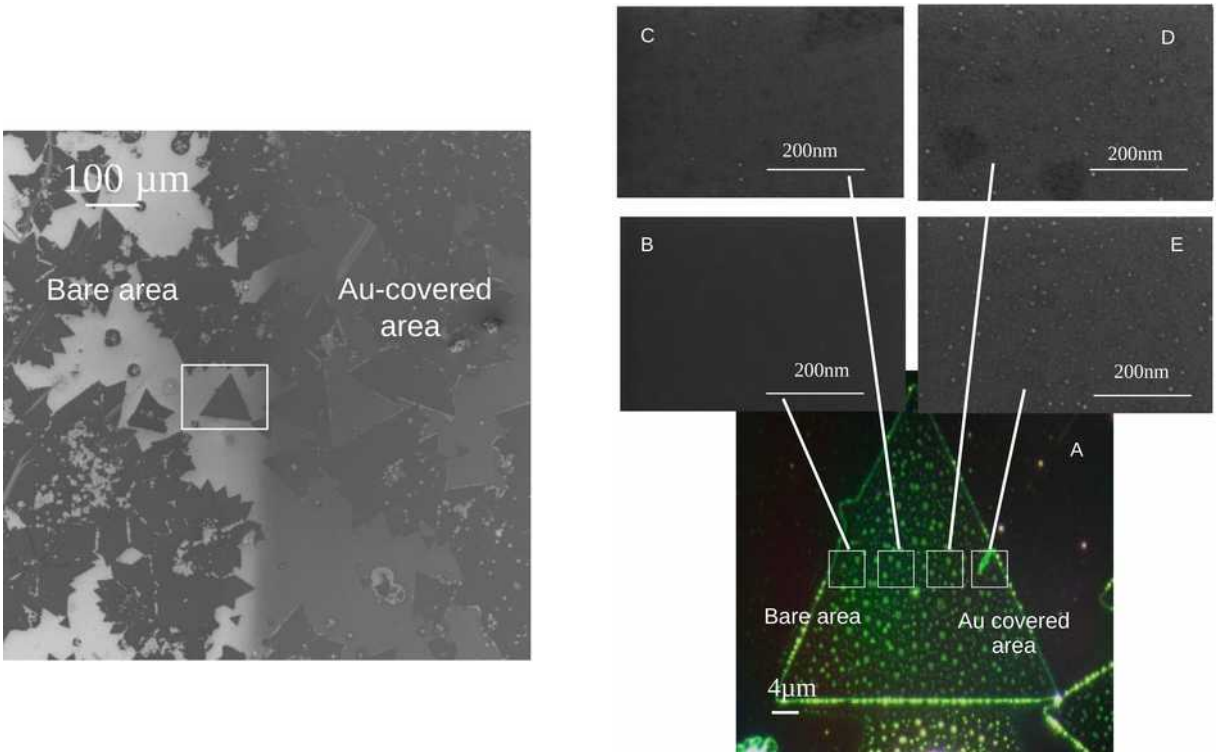

Figure A5: The SiO_2/Si substrate supporting the $MoSe_2$ flakes was partly masked prior to the deposition of Au (0.8 nm nominal thickness). Due to the rounded shape of the mask edge, the sputtered Au atoms slightly penetrate underneath the mask which is responsible for a non-abrupt transition from Au-covered to bare $MoSe_2$ regions.

Left figure: Scanning Electron Microscopy (SEM) image (×156 magnification) in the transition area between Au-covered and bare $MoSe_2$ regions of the sample. An isolated triangular $MoSe_2$ flake located in this area was selected for optical spectroscopy investigations.

Right figure: A) Dark field optical image (x50 magnification) of the selected $MoSe_2$ flake. B, C, D, E) SEM images (× 350000 magnification) recorded in the square delimited areas shown in A. The Au NPs are visible in the SEM images and their density clearly increases from left to right : 0.2 ± 0.1 % (C), 0.4 ± 0.1 % (D) and 0.7 ± 0.1 % (E)

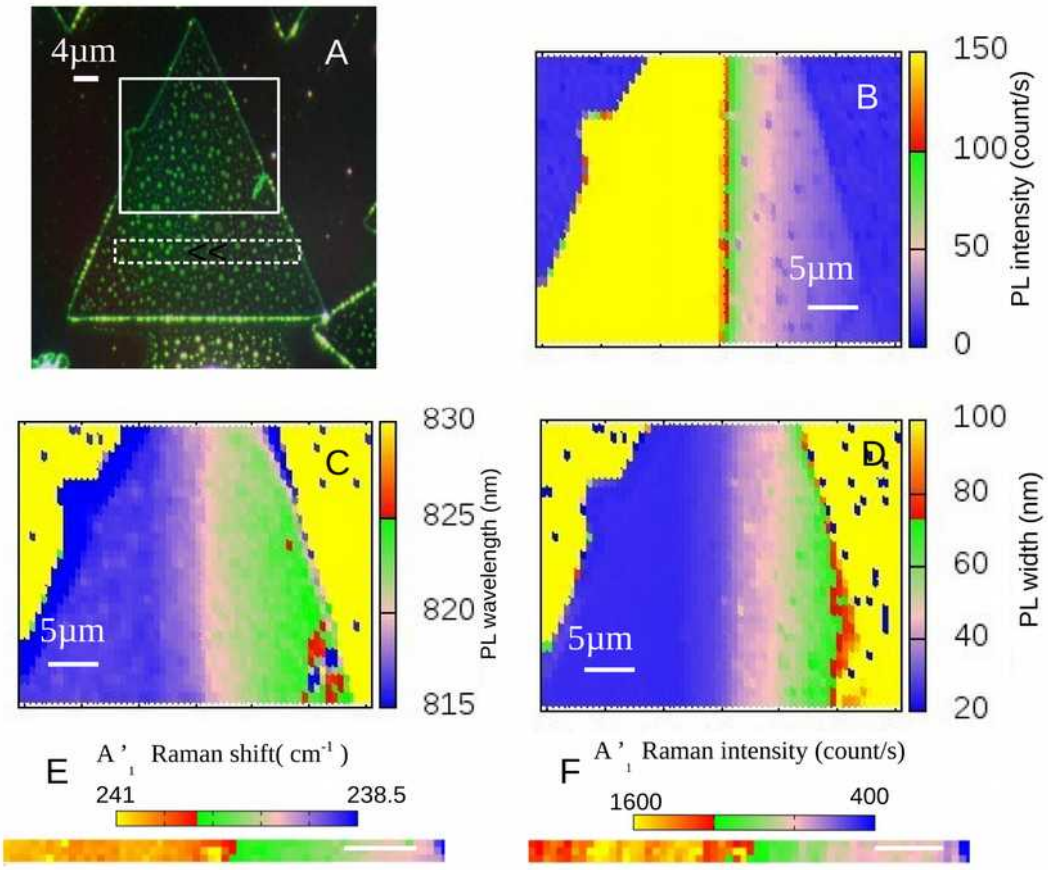

Figure A6: The SiO_2/Si substrate supporting the $MoSe_2$ flakes was partly protected by a mask prior to the deposition of Au (0.8 nm nominal thickness).

A) Dark field optical image (x50 magnification) of a $MoSe_2$ flake located in the transition area between Au-covered and bare $MoSe_2$ regions of the sample. B) Photoluminescence intensity, C) wavelength and D) linewidth mapped in the region delimited by the white square shown in A. The photoluminescence was excited by a 532 nm laser beam focused on the sample by a 0.9 NA objective (spatial resolution around 1 μm^2). The density of Au NPs and $MoSe_2$ surface coverage increases continuously from left to right (see Figure A5). As a consequence, the PL intensity increases (i.e., PL quenching is suppressed) with decreasing density of the Au NPs. Also, the PL emission wavelength blue shifts and its line width decreases due to weaker disorder effects caused by the Au NPs. E) Peak wavenumber and F) intensity of Raman scattering by A'_1 phonons mapped in the region delimited by the rectangular dotted line in Figure A. The quenching of both Raman scattering and PL emission are clearly correlated. The intensity of the Raman peak progressively increases (by approximately a factor 3) and its position blue shifts to its nominal value in monolayer $MoSe_2$ (around 241 cm^{-1}) with decreasing density of Au NPs. Both quenchings of the Raman scattering and PL emission are interpreted in terms of transfer of the photo-excited electron from the $MoSe_2$ layer to the Au NPs; the latter acting as traps for the photo-generated electrons.

Numerical simulations based on the Discrete Dipole Approximation method

Discrete Dipole Approximation (DDA) method has been used to calculate the electric near-field distribution generated by excitation (532 nm laser wavelength) of a hemispherical Au nanoparticle (17 nm in diameter) supported either by a 20 nm thick SiO_2 substrate or by a $MoSe_2$/SiO_2 layer with thickness increasing from 1 to 150 monolayers (i.e., bulk like $MoSe_2$) as shown in Figure 5. The calculations were implemented in DDSCAT 7.3.3 software [2-5]. The inter-dipole distance was set to 0.5 nm to ensure full convergence of the calculations while keeping within reasonable computation time. The optical index of Au was taken from ref [6] and those of $MoSe_2$ monolayer and SiO_2 from refs [7] and [8], respectively. The optical index of monolayer $MoSe_2$ was assumed in all the calculations and only the thickness of the layer was increased. This means that the effect of Van der Waals interlayer interaction on the electronic band structure and on the optical index of multilayer $MoSe_2$ was not taken into account.

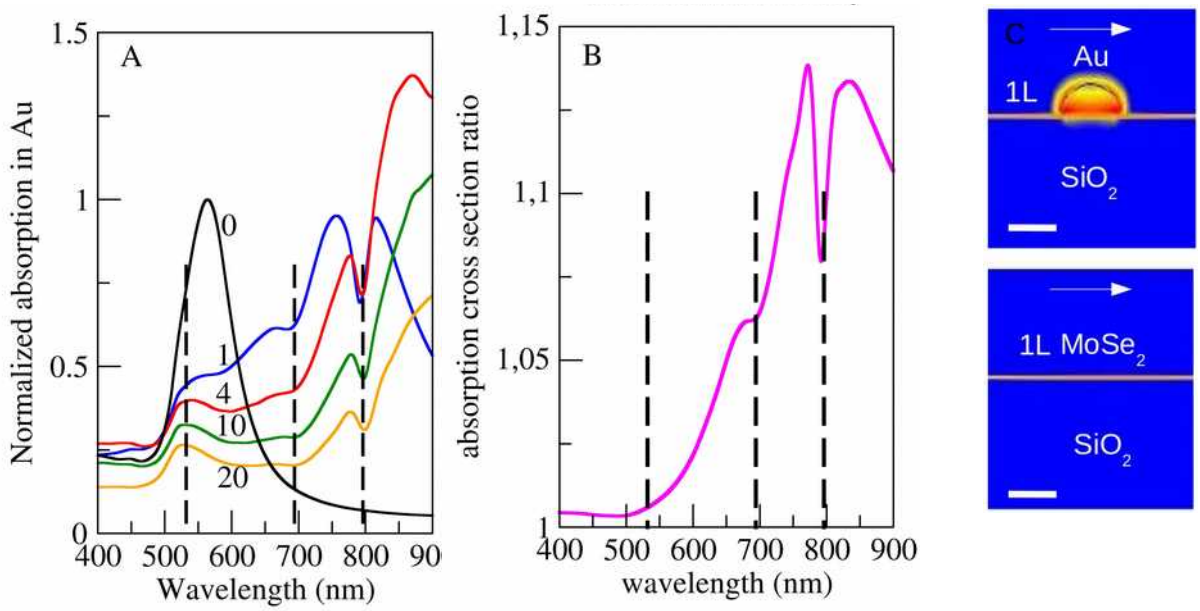

Figure A7: Discrete Dipole Approximation (DDA) based numerical simulations:

A) Optical absorption spectra of a hemispherical Au nanoparticle (17 nm in diameter) supported either by a 20 nm-thick SiO_2 substrate (spectrum labeled 0) or by a $MoSe_2$ multilayer flake stacked on a 20 nm-thick SiO_2 substrate. The thickness of the $MoSe_2$ flake is 1, 4, 10 and 20 monolayers. The absorption by the Au nanoparticle is calculated using a spatial integration of the electric field intensity enhancement (Figure 5) inside the nanoparticle and the imaginary part of the dielectric function of gold. The spectra are normalized to the maximum absorption of the Au nanoparticle on SiO_2. The dashed vertical lines indicate the A (796 nm) and B (694 nm) exciton wavelengths and the laser excitation wavelength (532 nm). The surface plasmon resonance of the Au nanoparticle on SiO_2 is strongly red-shifted, damped and hybridized with the excitonic transitions when the nanoparticle is supported by $MoSe_2$. The dips at the exciton wavelengths indicate a Fano type interaction between the plasmonic resonance and the A and B excitonic transitions.

B) Optical absorption spectrum of a monolayer $MoSe_2$ supporting a 17 nm hemispherical Au NP The absorption is calculated using a spatial integration of the electric field intensity enhancement inside the $MoSe_2$ layer and the imaginary part of the dielectric function of monolayer $MoSe_2$. The optical absorption spectrum is normalized with respect to the spectrum calculated for a bare monolayer $MoSe_2$. As the vertical axis scale starts at 1, the optical absorption of the $MoSe_2$ layer is clearly enhanced by the Au NP, particularly around the dips formed by the Fano interference between the plasmonic resonance and the A and B excitonic transitions.

C) Electric field intensity enhancement $|E|^2/|E_0|^2$ calculated for a hemispherical 17 nm diameter Au NP on monolayer $MoSe_2/SiO_2$ and for bare monolayer $MoSe_2/SiO_2$. The thickness of the SiO_2 substrate is 20 nm. The scale bar is 10 nm long and the arrow indicates the polarization of the incident electric field. Calculations were performed for 532 nm wavelength corresponding to the laser wavelength used to excite the PL emission. The intensity is in log scale and the maximum intensity (red) is for 0.4.

Calculations of the optical reflection properties of $MoSe_2/SiO_2/Si$ and SiO_2/Si stacks

To estimate the impact of the $MoSe_2$ layer on the optical properties of the substrate, the optical reflection properties of $MoSe_2/SiO_2/Si$ and SiO_2/Si 2D stacks were calculated using the scattering

matrix method[9]. The latter is well adapted to the analysis of interference effects in layered 2D systems. Since the PL emission from the Au NP involves d-to-s transition dipole momentum and that the deposited Au nano-crystals are randomly oriented, we assume that the emission of the hemispherical Au nanoparticle is isotropic (random orientation of the transition dipole) and that half of the light intensity is emitted by the air-exposed surface and directly collected by the objective. The other half (directed towards the substrate) is subject to interference effects produced by the optical cavity formed by the (0.8 nm) $MoSe_2$/(90 nm)SiO_2/Si stack (Figure A8). We used complex refractive indexes from literature for $MoSe_2$[7], SiO_2[8] and Si [10]

To match the experimental conditions, we considered the average reflection of the emitted light for incident angles between 0° (normal incidence) and 65° corresponding to 0.9

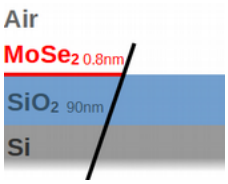

numerical aperture of the collection objective of our setup. As the light emitted by the Au NPs is not polarized, we also averaged the reflected spectra over the transverse electric (TE) and transverse magnetic (TM) polarizations. Figure A8 shows the spectrum of the ratio of the reflection coefficients calculated with and without the $MoSe_2$ layer. The average value of this ratio is below 1 which indicates that the addition of the $MoSe_2$ layer decreases the amount of the light reflected by the substrate. This reduction in reflectivity (between 0.94 and 0.97 in the

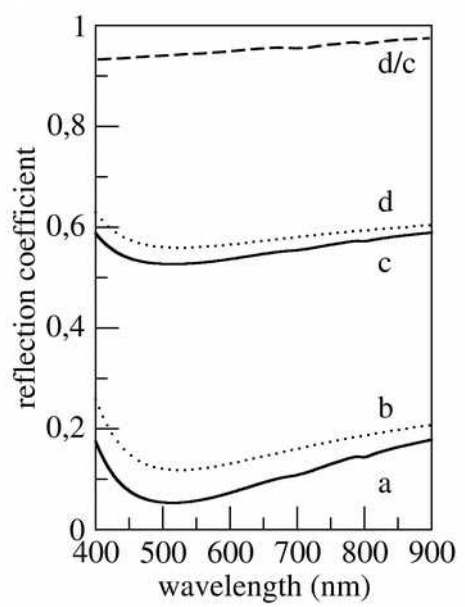

PL emission range of the Au NPs) is rather weak which indicates that interference effects do not play a major role, mainly because of the large numerical aperture of the objective which operates an angular averaging of the collected signal.

Figure A8: a) and b) reflectivity spectra of $MoSe_2$/SiO_2/Si (full lines) and SiO_2/Si (dotted

lines) stacks (right figure) calculated using the scattering matrix method. The spectra were integrated over the angular dispersion for numerical aperture NA=0.9 and TE/TM polarizations. c) and d) are reflectivity spectra corrected assuming that 50% of the emitted light is reflected by the substrate. The other 50% is directly collected by the objective. The dashed line shows the ratio d/c of spectra d) and c).

References

[1] Carles, R.; Benzo, P.; Pécassou, B.; Bonafos, C. Vibrational Density of States and Thermodynamics at the Nanoscale: The 3D-2D Transition in Gold Nanostructures. *Scientific Reports* **2016**, *6*, srep39164.

[2] Goodman, J. J.; Draine, B. T.; Flatau, P. J. Application of Fast-Fourier-Transform Techniques to the Discrete-Dipole Approximation. *Opt. Lett., OL* **1991**, *16* (15), 1198–1200.

[3] Draine, B. T.; Flatau, P. J. Discrete-Dipole Approximation For Scattering Calculations. *J. Opt. Soc. Am. A, JOSAA* **1994**, *11* (4), 1491–1499.

[4] Flatau, P. J.; Draine, B. T. Fast near Field Calculations in the Discrete Dipole Approximation for Regular Rectilinear Grids. *Opt. Express, OE* **2012**, *20* (2), 1247–1252.

[5] Draine, B. T.The Discrete-Dipole Approximation and Its Application to Interstellar Graphite Grains. *The Astrophysical Journal* **1988**, *333*, 848–872.

[6] Johnson, P. B.; Christy, R. W.
Optical Constants of the Noble Metals. *Phys. Rev. B* **1972**, *6* (12), 4370–4379.

[7] Liu, H.-L.; Shen, C.-C.; Su, S.-H.; Hsu, C.-L.; Li, M.-Y.; Li, L.-J. Optical Properties of Monolayer Transition Metal Dichalcogenides Probed by Spectroscopic Ellipsometry. *Appl. Phys. Lett.* **2014**, *105* (20), 201905.

[8] Palik, E. D.*Handbook of Optical Constants of Solids*; Academic Press: Orlando, 1985.

[9] D. Y. K. Ko et J. R. Sambles, Scattering matrix method for propagation of radiation in stratified media: attenuated total reflection studies of liquid crystals, *JOSA A, 1988*, vol. 5, n° 11, p. 1863–1866

[10] Schinke, C.; Christian Peest, P.; Schmidt, J.; Brendel, R.; Bothe, K.; Vogt, M. R.; Kröger, I.; Winter, S.; Schirmacher, A.; Lim, S.; Nguyen, H. T.; MacDonald, D. Uncertainty Analysis for the Coefficient of Band-to-Band Absorption of Crystalline Silicon. *AIP Advances* **2015**, *5* (6), 067168.